

Simulation of an isolated Wind Diesel System with battery energy storage

R. Sebastián*, R. Peña Alzola

Department of Electrical, Electronic and Control Engineering, Spanish University for Distance Education, 28040 UNED Madrid, Spain

ARTICLE INFO

Article history:

Received 23 March 2010
Received in revised form 6 August 2010
Accepted 26 October 2010

Keywords:

Wind Diesel
Isolated Power Systems
Dynamic simulation
Battery based Energy Storage Systems
Current Controlled Inverter

ABSTRACT

The subject of this paper is to present the modelling and simulation of an isolated Wind Diesel Hybrid System (WDHS) comprising a Diesel Generator (DG), a Wind Turbine Generator (WTG), the consumer Load, a Ni–MH battery based Energy Storage System (BESS) and a Dump Load (DL). The BESS consists of a battery bank and a power converter which performs the DC/AC conversion to interface the battery with the isolated grid. The Ni–MH battery high power capability, low maintenance, resistance to abuse and absence of hazardous substances make it the best choice for WDHS. The modelling of the previously mentioned components is presented and the performance of the WDHS is tested through dynamic simulation. Simulation results with graphs for the frequency and voltage of the Isolated Power System, active powers generated/absorbed by the different elements and the battery voltage/current/state of charge are presented for load and wind speed changes. The simulation results for the BESS/no BESS cases are compared and show a remarkable improvement in the system dynamics due to the use of the BESS.

© 2010 Elsevier B.V. All rights reserved.

1. Introduction

A Wind Diesel Hybrid System (WDHS) is any autonomous electricity generating system using Wind Turbine Generator(s) (WTG) with Diesel Generator(s) (DG) to obtain a maximum contribution by the intermittent wind resource to the total power produced, while providing continuous high quality electric power [1]. The main aim with these Isolated Power Systems is to reduce fuel consumption and in this way, to reduce system operating costs and environmental impact. If the WDHS is designed so that the diesels have to run full time, the WDHS is classified as being low or medium wind penetration depending on the Energy Penetration ratio of the wind power [2], defined as:

$$\text{Energy penetration} = \frac{\text{Wind Turbine annual energy output (kWh)}}{\text{Annual primary energy demand (kWh)}} \quad (1)$$

The WDHS is classified as low penetration when (1) is less than 20% and as medium penetration when (1) is between 20% and 50%. Conversely if the WDHS is capable of shutting down the Diesel Generators during periods of high wind availability, the WDHS is classified as being high wind penetration. Fig. 1 shows the medium penetration WDHS studied in this paper where the components stated in the definition of the WDHS can be seen: the DG, the WTG and the consumer load. Other components shown in Fig. 1 such as Dump Loads (DL) or Battery Energy Storage Systems (BESS) are explained in Section 2.

Several papers have been published on the subject of WDHS dynamic simulation. In [3] a no-storage WHDS is simulated against several perturbations, among them the connection of a WTG to the DG isolated grid. In [4], the modelled WDHS includes a variable speed flywheel energy storage based on hydrostatic transmission. In [5], the simulated high penetration WDHS has a DG with a clutch which allows disengaging the Diesel Engine (DE) from the synchronous machine (SM) when the generated wind power exceeds the consumed load power. This paper focuses on the dynamic simulation of a medium penetration WDHS and the dynamic improvement that produces to include a BESS in the system. After this introductory Section 1, this article is organized as follows: Section 2 presents the WDHS architecture discussed in this article along with its control requirements, Section 3 presents the control system that has been used, Section 4 shows the modelling of the WDHS components, Section 5 presents the WDHS response against different perturbations and finally Section 6 emphasizes the effectiveness of using the BESS.

2. WDHS architecture and operation modes

The Medium penetration WDHS of Fig. 1 comprises one DG and one WTG and has two operation modes: Diesel Only (DO) and Wind Diesel (WD). In DO mode the DG supplies the active and reactive power demanded by the consumer load (in this mode the WTG is shut off so $C_T = \text{OFF}$ in Fig. 1). The speed governor (speed regulator + actuator) controlling the DE, performs frequency regulation and voltage regulation is performed by the automatic voltage regulator in the SM. In WD mode, the WTG also supplies active power and the same regulators as in DO mode are in charge of the fre-

* Corresponding author.

E-mail address: rsebastian@ieec.uned.es (R. Sebastián).

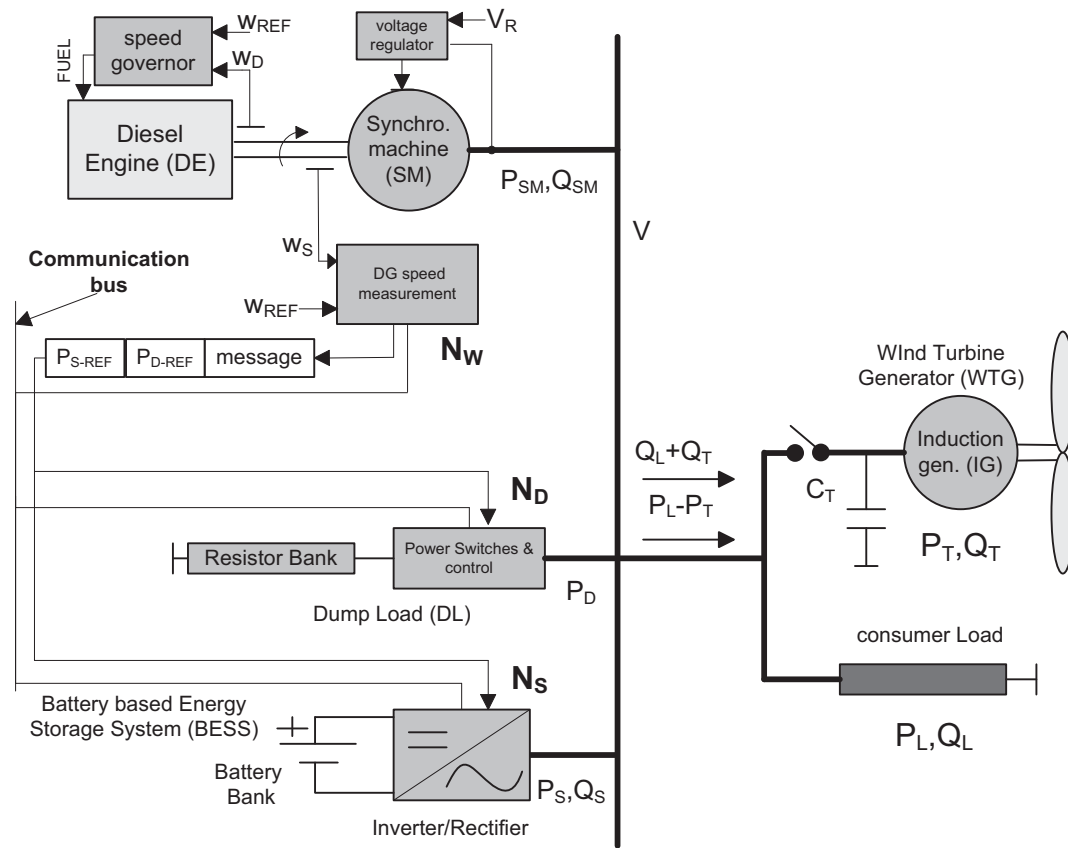


Fig. 1. Layout of the isolated medium penetration WDHS and the DCS.

quency and the voltage control (referring to Fig. 1, $C_T = \text{ON}$ in WD mode).

The DE speed control in Fig. 1 is isochronous so the diesel speed governor will command the necessary fuelling rate to make the DE run at constant speed. The DG under the control of the speed governor performs the frequency regulation by maintaining an instantaneous balance between the consumed and produced active power. Therefore, the DE behaves as a controlled source of active power.

The WTG in Fig. 1 consists of a Wind Turbine (WT) driving an Induction Generator (IG) directly connected to the autonomous grid conforming a constant speed stall-controlled WTG (no pitch control). The mechanical power produced by a WT [6] is:

$$P_{T-MEC} = \frac{1}{2} \rho A v^3 C_p \quad (2)$$

where ρ is the air density, v is the wind speed, A is the area swept by the turbine blades and C_p is the power coefficient. C_p is a function of the Tip Speed Ratio ($\text{TSR} = R\omega_r/v$, where R is the blade length and ω_r is the WT shaft speed) and the blade pitch. Since the WTG used in this paper has no pitch control C_p is only a function of TSR. In addition, the IG speed range variation in the WTG is very limited and thus C_p can be considered as a function only of the wind speed. As the wind speed is quasi-random there is no way to control the WTG active power, so the WTG behaves as an uncontrolled source of active power. The IG consumes reactive power so a capacitor bank has been added to compensate the power factor.

In WD mode, the WTG produced power P_T can be greater than the load consumed power P_L , so in this case the outgoing active power from the isolated power plant $P_L - P_T$ is negative. This situation means that the DG power must be negative (DG power inversion) to balance active powers (consumption = production) in

order to keep frequency constant. Since the speed governor cannot order the DE to consume power, the DG is unable to regulate frequency when $P_L - P_T < 0$. To avoid the DG power inversion, a Dump Load (DL) [7] must be incorporated to the system. The WDHS control will order to the DL to dump the necessary power to keep the needed DG produced power positive, so that the DG can regulate the frequency. The DL in Fig. 1 consists of a set of power switches and a bank of resistors. By closing/opening these power switches, the DL consumed active power can be controlled and thus the DL behaves as a controlled sink of active power.

An Energy Storage System (ESS) [7] can also be used to prevent the DG power inversion in WD mode. Additionally ESS can be used in both DO and WD modes to reduce the spinning reserve needs, to increase the loading of the DGs in order to improve their performance and to improve the dynamics of the WDHS as it will be seen later. The Battery based Energy Storage System (BESS) of Fig. 1 consists of a battery bank and a power converter which performs the DC/AC conversion to interface the battery bank with the autonomous grid. The BESS can store or retrieve power as needed, so it behaves as a controlled sink/source of active power. A review on BESS can be seen in [8]. In [9] a BESS is used for smoothing the generated power by a wind farm.

3. The control system

A Distributed Control System (DCS) is proposed to control the DL and BESS in the presented power system. A DCS [10] comprises several CPU based electronic control units (also called nodes) physically distributed and linked by a communication network (also called communication bus). As it can be seen in Fig. 1, the proposed DCS consists of three nodes: a DG shaft speed measurement sensor node N_W and two actuators nodes: the DL converter N_D and the

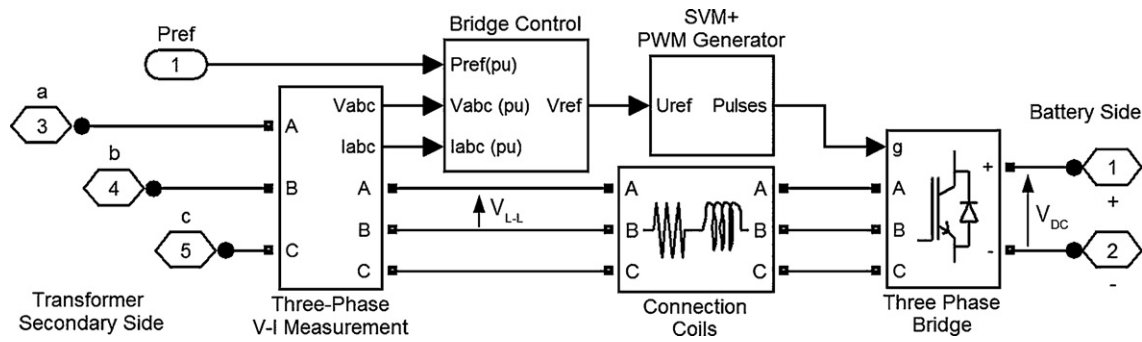


Fig. 3. CCI Simulink-SimPowerSystems schematic.

1 voltage regulator plus an exciter regulates the voltage in the SM terminals.

The constant speed stall controlled WTG [14] comprises an Induction Generator (IG) of 275 kW (WTG rated power $P_{T-NOM} = 275$ kW) directly connected to the autonomous grid and the Wind Turbine (WT) block. The electrical part of the IG is represented by a fourth-order model. The WT block contains the Wind Turbine power curves which define the mechanical power in the WT shaft as a function of the wind speed and the WT shaft speed as it is described in Eq. (2). The WT mechanical power is divided by the WT shaft speed to calculate the input torque applied to the IG. This WTG has no pitch control, so there is no way to control the power it produces.

The high order SM (6th order) and IG (4th order) models are used in order to obtain precise voltage dynamics during simulation. WDHSs use small machines [15] and therefore, are low inertia Isolated Power Systems where significant frequency deviations occur. Normally power system stability studies use reduced order models to increase the maximum integration step size. Apart from faster simulation speed, this results in smothered waveforms when compared to those resulting from full order models. Power system stability studies are primarily interested in the electromechanical dynamics of large electric machines. According to [16] if the machines are small in horsepower or if the machines are operated over a relatively wide frequency range, as it is the case of WDHS [15], reduced order models should not be used without first comparing to the full order models. Previous simulations of high penetration WHDS confirmed the necessity of using full order models [17], so that full order models for the SM and the IG were used in the present simulations.

The consumer load consists of a 175 kW main load and a 100 kW extra load (both resistive) which can be connected/disconnected by closing/opening the 3 Phase Breaker (3PB) in Fig. 2. The 175 kW represents the WDHS average load and the total 275 kW is considered

the WDHS maximum load, so that when 3PB changes from opened to closed, the system load increases suddenly from its average value to its maximum one. The ratio average load/maximum load used in this paper is close to the typical 2/3 of the daily load pattern of WDHS [18].

The Dump Load consists [14] of eight three phase resistors connected in series with GTO switches. The resistor values follow an 8 bit binary progression so that the power consumed by the DL, provided rated grid voltage, can be expressed in the form:

$$(S_0 + S_1 \cdot 2^1 + \dots + S_7 \cdot 2^7) \cdot P_{STEP} = X_{D-REF} \cdot P_{STEP} \quad (6)$$

(6) means that the power can be varied discretely from 0 to $255 \cdot P_{STEP}$, where P_{STEP} is the power corresponding to the least significant bit ($X_{D-REF} = 0-255$, $P_{STEP} = 1.4$ kW, $P_{D-NOM} = 357$ kW), and S_j is "1" when the associated GTO is turned on and "0" when the GTO is turned off. The DL rated power P_{D-NOM} was chosen to be a 30% greater than P_{T-NOM} , so that the power inversion case commented in Section 2 can be controlled even in the case of no consumer load and BESS fully charged/failure.

The BESS is based on a Ni–MH battery bank, a LC filter, an IGBT three-phase bidirectional Current Controlled Inverter (CCI) of rated power $P_{S-MOM} = 150$ kW and a 150 kVA elevating transformer.

The elevating transformer isolates the three phase power inverter and the battery bank from the autonomous grid. Its rated line to line voltage in the grid/inverter sides are 480/120 VAC.

The CCI receives its active power reference P_{S-REF} from the power sharing block. P_{S-REF} can be established for inverter mode operation (the CCI supplies power to the isolated grid and discharges the battery), or rectifier mode operation (the CCI absorbs power from the isolated grid and charges the battery). Although the CCI can control the reactive power it consumes/produces its reference reactive power is set to 0.

The voltage source CCI schematic in Simulink, by using elements of the SimPowerSystems library, is shown in Fig. 3. The Discrete

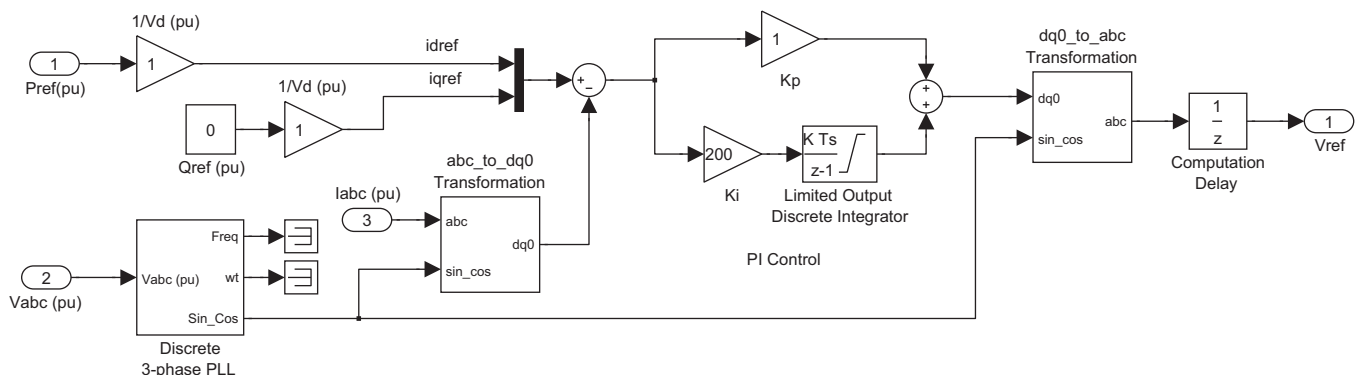


Fig. 4. CCI current control schematic.

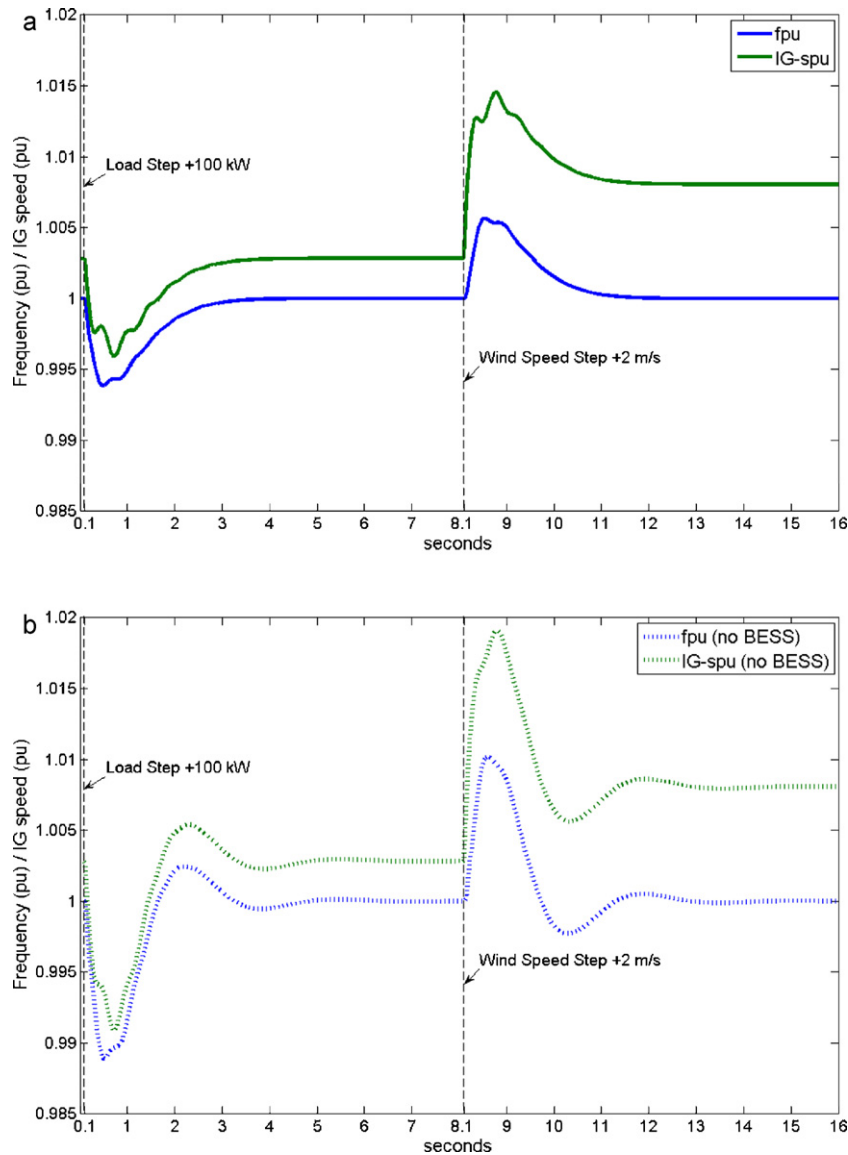


Fig. 5. (a) Frequency per unit and IG speed per unit in the BESS case. (b) Frequency per unit and IG speed per unit in the NO BESS case.

PWM generator commands the IGBTs in the three phase bridge at a switching frequency of 5 KHz. Three inductances of 3.8 mH (1.8 mH of the equivalent transformer leakage inductances and 2 mH of the inverter coil inductances, both magnitudes referred to the transformer primary side) limit the harmonic current injection to the grid.

The current measurement block measures the three output CCI phase currents (I_a , I_b and I_c) in pu. The current sampling is synchronous to the converter PWM carrier peaks in order to optimize the current control bandwidth [19]. The main advantage of synchronous current sampling is that it is not necessary to use heavily attenuated low-pass filters in order to remove PWM current ripple. These filters have a decreasing effect in the control dynamics due to their inherent delay. Current control in the CCI is performed in the rotating dq-coordinate frame [20] as seen in Fig. 4. This framework is synchronous to the grid voltage so, assuming perfect orientation, the voltage direct component is equal to the voltage amplitude $V_d = V$ and the voltage quadrature component is null $V_q = 0$. The discrete three phase PLL (phase locked loop) block tracks the variable frequency grid voltage waveform providing the reference for both abc-dq and dq-abc coordinate transformations. The

CCI output phase currents are transformed to the rotating frame by the abc_to_dq0 transformation block. In this rotating dq-coordinate framework the current direct component i_d controls active power, $P = i_d \cdot V$, provided perfect orientation. In an analogous manner current quadrature component controls reactive power, $Q = i_q \cdot V$. Grid voltage V remains close to 1 pu so active power will be equal to approximately direct current in pu. Grid voltage V variations are not taken into account in the current control since it would result in harmonic injection to the grid. Also in an analogous manner current quadrature component in pu will be equal approximately to reactive power in pu. Therefore by setting i_{q-ref} to zero the CCI achieves unity power factor. To establish direct and quadrature current references simple Proportional Integral (PI) controls are used with limited integration in order to avoid integrator windup. With $K_p = 1$, $K_i = 200$ and a $50 \mu s$ sample time for both direct current (i_d) and quadrature current (i_q) PI controls, the CCI P_{S-REF} step response time is less than 1 ms. The PI controller outputs are transformed back to phase quantities to be compared with the triangular carrier waveform in order to establish the necessary phase voltages.

Battery voltage level is determined by three phase converter power constraints since battery works as the DC-link. Accounting

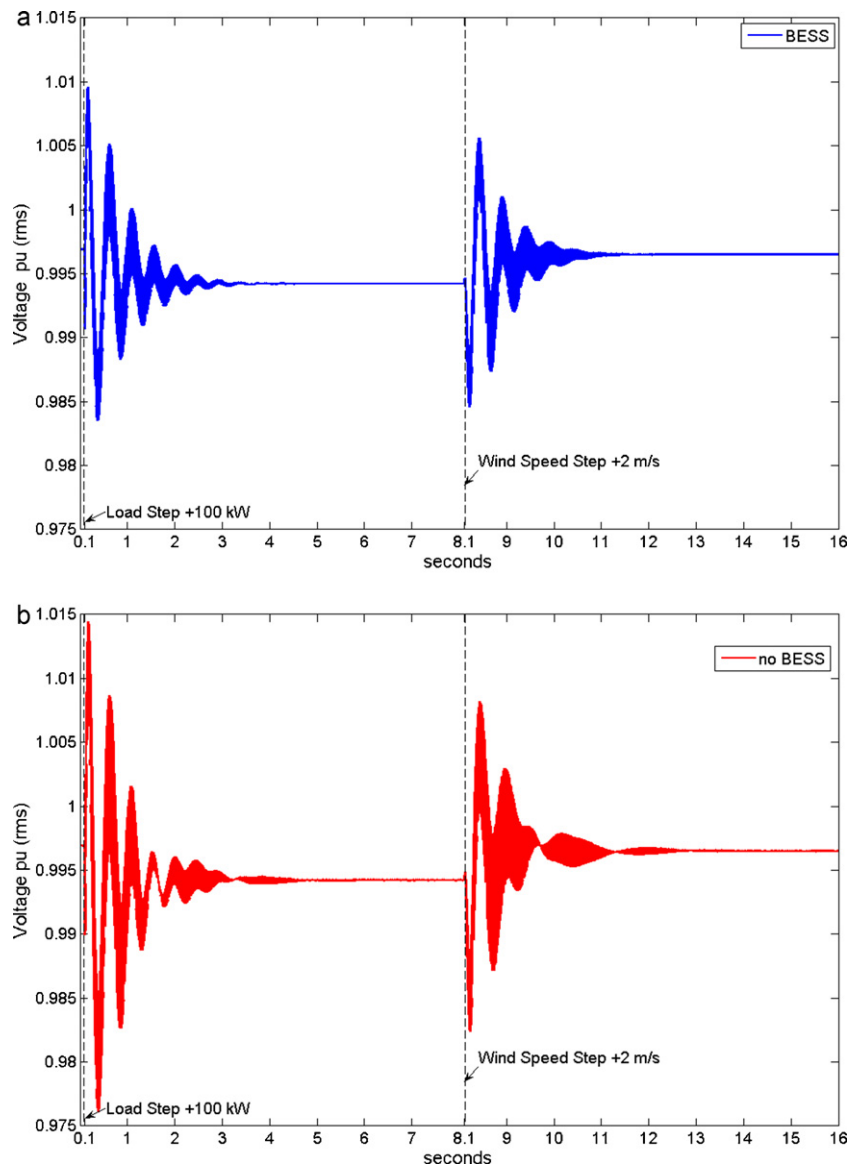


Fig. 6. (a) RMS Voltage per unit in the BESS case. (b) RMS Voltage per unit in the NO BESS case.

for grid fluctuations, line reactor voltage drop and operation reliability, the DC-link voltage should be selected above 10–15% of the natural DC-link voltage [21]. Natural DC-link voltage is defined as the voltage obtainable if the semiconductor switches are not operating and the converter works as a standard free-wheeling diode bridge [21]. Natural DC-link voltage corresponds to the peak value of the line to line voltage. Hence, referring to Fig. 3, DC-link voltage V_{DC} level should be selected as:

$$V_{DC} = 1.10 \div 1.15 \sqrt{2} V_{L-L} \quad (7)$$

where V_{L-L} is the line to line RMS voltage. If DC-link voltage is smaller than the natural DC-link voltage, the bridge diodes will charge the battery, and the semiconductor switches will discharge it. This will result in a reactive current flowing between the grid and the converter. Moreover, Eq. (7) should be also verified for the expected grid voltage variations. To assess the validity of the selected DC-link voltage level, the amplitude of the converter output voltage must comply also with Eq. (8) for unity power factor, neglecting the line resistive drop, in order to be in the linear mod-

ulation region:

$$m \frac{V_{DC}}{2} > \sqrt{\frac{2}{3} (V_{L-L})^2 + (\omega L i_d)^2} \quad (8)$$

where m is the modulation index, ω is the grid pulsation, L the connection coil inductance and i_d the current direct component defined previously. Right side of (8) is the phase to neutral converter voltage peak value due to the grid connection by means of an inductor. Left side of (8) reflects the fact that the PWM converter behaves as an ideal voltage source in the linear region. Modulation index m can be as high as 1 for the sinusoidal modulation and as high as $2/\sqrt{3}$ for the space vector modulation. Space vector modulation is used most often because it allows a better DC-link utilization. Indeed, it has an easy digital implementation and results in low ripple current. Thus, space vector modulation was chosen to be used in the presented simulation. The selected standard battery voltage value $V_{DC} = 240$ V is larger than the one resulting from (7), avoiding operation as diode bridge. It also allows supplying the rated power, 150 kW, fulfilling Eq. (8) even with an increase of 6% in the grid voltage (see Appendix for calculations).

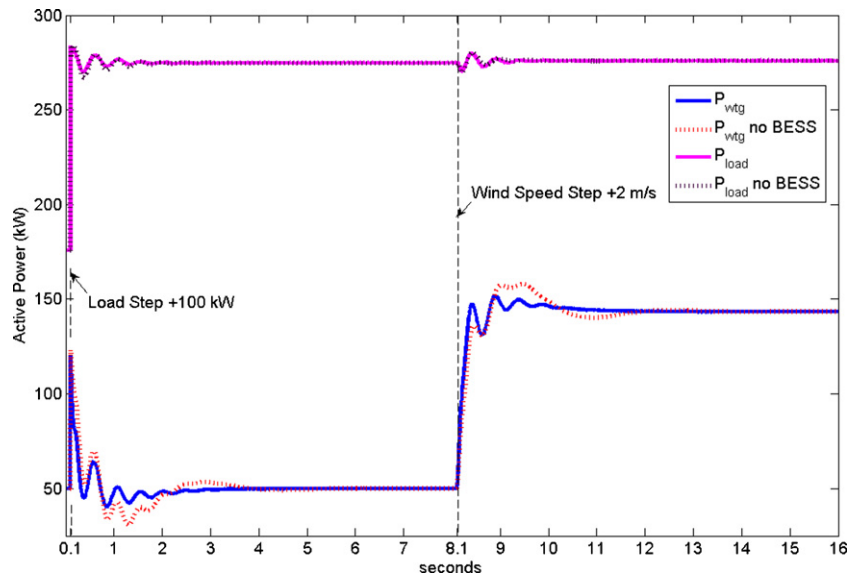


Fig. 7. WTG produced and load consumed active powers.

Ni–Cd batteries are preferred to Lead acid type in short term BESS for isolated WDHS [22]. Also in the near field of Uninterrupted Power Supplies UPS [23], Ni–Cd batteries are always used when the working UPS conditions are extreme and/or maintenance is difficult. Ni–Cd batteries useful lifetime is four times larger than that of the Pb-acid type and with lower maintenance costs [24], very valuable features in remote areas. Ni–Cd batteries have also greater power capability, so that for a given power converter, Ni–Cd batteries need one-third the ampere-hour capacity needed in case of using Pb-acid type [24]. In addition, in a WDHS the battery current may be continuously changing, even changing from charging to discharging and back again. Ni–Cd batteries are also superior in this issue as they can sustain more charging/discharging cycles than Pb-acid type. These considerations pay off the greater initial cost of the Ni–Cd. Ni–MH batteries have very similar properties to Ni–Cd batteries, using hydrogen-absorbing alloy for the negative electrode instead of cadmium. Ni–MH batteries have shorter useful lifetime, but more power capability than Ni–Cd type [24]. Cadmium is a toxic heavy metal with mandatory provisions for disposal not so easy to fulfil in remote areas. Therefore, this environmental aspect recommends selecting Ni–MH batteries for this present article. The 240 V Ni–MH battery model [25] consists of a DC voltage source function of the state of charge (SOC), based on the discharge characteristic of the battery, and an internal resistance of assumed constant value. The energy stored in the battery is 93.75 kWh, which is obtained from a storage energy need during 15 min for the 150 kW rated power CCI and with the Ni–MH battery operating between 35% and 75% of its rated capacity ($150 \text{ kW} \cdot 15 \text{ min} / (0.4 \cdot 60 \text{ min/h}) = 93.75 \text{ kWh}$) [17]. This 93.75 kWh corresponds to a capacity C of 390.625 Ah ($93.75 \text{ kWh} / 240 \text{ V} = 390.625 \text{ Ah}$) in the 240 V Ni–MH battery. Finally, the LC filter of Fig. 2 smoothes the battery current by reducing the current ripple coming from the DC side of the CCI.

The N_W node in Fig. 1 is simulated by means of the Active Power Regulator (APR) and the Power Sharing blocks in Fig. 2. The APR receives the SM shaft speed per unit (pu) as input (which is equal to the system frequency pu) and outputs the needed P_{REF} to the BESS/DL Power sharing block. The APR applies a discrete version of Eq. (3) with a 2.5 ms sample time. This 2.5 ms sample time sets the 400 Hz transmission frequency for the P_{REF} message in Fig. 1. The proportional and derivative gains K_P and K_D (values given in

the Appendix) of Eq. (3) has been chosen to position the dominant pole pair of the WDHS linearized model to be a double pole in order to increase speed response and minimise the over/under shooting. Since the pure derivative term of Eq. (3) would amplify measurement noise, a lead compensator in the form $\alpha \cdot T_d \cdot s / (1 + \alpha \cdot T_d \cdot s)$ with $\alpha = 0.1$ and converted into the z equivalent has been used.

The BESS/DL sharing defined in (4) and (5) is performed within the Power Sharing Block in Fig. 2. When $P_{REF} > P_{S-NOM}$, this block assigns to the DL the minimum integer number X_{D-REF} which verifies $X_{D-REF} \cdot P_{STEP} > P_{REF} - P_{S-NOM}$ and after this, P_{S-REF} is defined as $P_{S-REF} = P_{REF} - X_{D-REF} \cdot P_{STEP}$. With these calculations (4) and (5) are always satisfied and the value of P_{S-REF} is accommodated to take into account the discrete nature of the DL used in this simulation (the DL consumed power can only vary discretely in multiples of P_{STEP} kW).

5. Simulation results

In the following paragraphs the WDHS response to a +100 kW consumer load and +2 m/s wind steps is presented. These sudden load and wind speed changes will not happen in a real system. Load variation is expected to be more progressive and also wind turbulence and gusts are smoother than a step variation. So both tests must be considered as the worst case in order to test the validity of the isolated system. The WDHS response is shown by graphs of the following variables: the system frequency pu (fpu) and WTG IG speed pu (Figs. 5A–5B), the RMS voltage per unit (Figs. 6A–6B), the active powers generated by the WTG and consumed by the load (both are non-controllable) (Fig. 7), and the active powers generated by the DG and generated/consumed by the BESS (both are controllable) (Fig. 8). For the WTG, DG and BESS the active power is considered positive if produced and for the load positive if consumed. Figs. 5A–6A and 5B–6B are the WDHS responses for the BESS/no BESS case respectively. In Figs. 5, 7 and 8, the dotted curves refer to the temporary evolution of the variables when the BESS is turned off and the solid line curves when the BESS follows the active power reference P_{REF} sent by block APR. The active power consumed by the DL is zero throughout the presented tests as P_{REF} is always below P_{S-NOM} . At the test starting point the wind speed is 7 m/s, the WTG and DG are producing active powers of 50 kW and 125 kW respectively, the load and BESS are consuming active

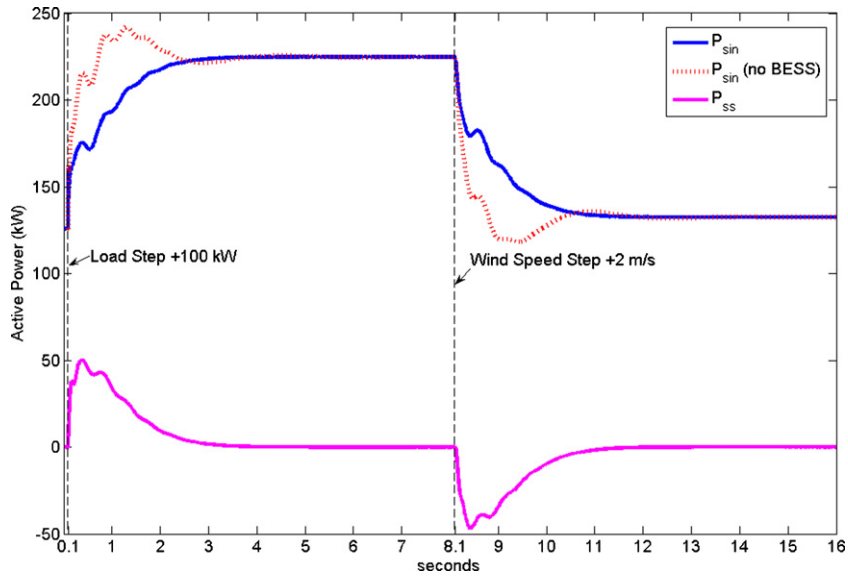


Fig. 8. DG and BESS produced active powers.

powers of 175 kW and 0 kW respectively and the battery SOC is 50%.

In $t = 0.1$ s the extra 100 kW resistive load is connected to the system (33% of the DG rated power) by closing the three-phase switch (3PB) in Fig. 2, as it can be observed in the load active power curve in Fig. 7, which also shows that the load power oscillates. The reason for these oscillations is that the load is purely resistive and as Figs. 6A–6B show, the voltage in the isolated grid is affected by the positive load step of 100 kW. The minimum–maximum voltages during this load step are 0.9835–1.0096 pu and 0.9761–1.0144 pu for the BESS/no BESS case respectively, so the variations are larger if there is no BESS. Also Fig. 7 shows that the wind power presents a transient due to the connection of this extra load, being again more oscillating if there is no BESS action. Figs. 5A–5B show that the system frequency reduction after the load step contributes to increase sharply the difference between the IG speed and the fpu (IG slip). This makes the WTG to instantaneously increase power production at expense of its kinetic energy as Fig. 7 shows. This is a desirable effect since counter acts the frequency dip by provid-

ing more power to the grid. In steady state the wind power has the same value as the initial one in $t = 0$, since the wind speed has not changed. Figs. 5A–5B show that the fpu/IG speed minimums are 0.9938 (–0.62%)/0.9959 with BESS action and 0.9889 (–1.11%)/0.9908 without BESS, being in addition in this second case, both responses over oscillating. Fig. 8 shows that the power in the DG is monotonically increasing in the BESS case and has an oscillation peak of 241.96 kW in the no BESS case. Fig. 8 also shows that the BESS generates active power throughout the transient due to the load step, being its steady state value null since the system reaches the equilibrium. In steady state reached at $t = 4.454/7.716$ s in the BESS/no BESS case, the DG assumes the increase of load with a final power of 225 kW.

In $t = 8.1$ s the wind speed changes suddenly from its initial value of 7 m/s to 9 m/s. Figs. 5A–5B show that the IG slip increases, but its variation is smoother than in the load step case since in this case the system frequency increases and part of the captured wind power is converted in WTG kinetic energy. Fig. 7 shows the corresponding increasing in the WTG power from its initial value to 143 kW

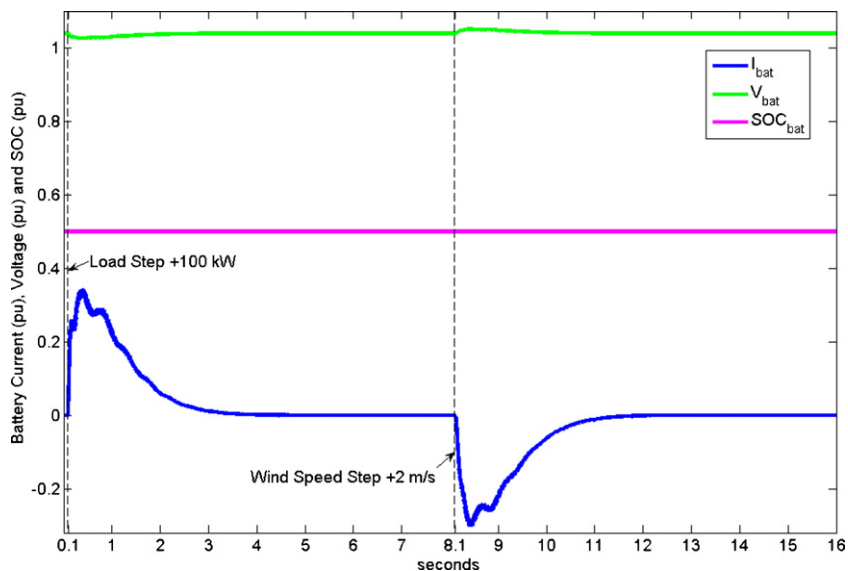


Fig. 9. Normalized battery current, voltage and SOC.

in steady state, faster and with oscillations of smaller amplitude in the BESS case. Figs. 5A–5B show f_{pu}/IG speed maximums of 1.0056 (+0.56%)/1.0145 in the BESS case and 1.0102 (+1.02%)/1.0191 in the no BESS case, being, in addition, both responses under oscillating in the no BESS case. The minimum–maximum voltages during this wind step are 0.9846–1.0056 pu and 0.9824–1.0082 pu for the BESS/no BESS case respectively. Fig. 8 shows that the DG power is monotonically decreasing in the BESS case and exhibits an under oscillation peak of value 118.16 kW in the no BESS case. Fig. 8 also shows that the BESS consumes active power throughout the transient due to the wind speed step. In steady state, reached at $t = 12.42/15.75$ s for the BESS/no BESS case, the BESS power is null and the DG accommodates its output power to the new situation generating 132 kW.

The battery SOC in pu, voltage normalized to its 240 V rated voltage, and current normalized to its 625 A rated current (150 kW/240 V = 625 A) are shown in Fig. 9. The battery current is considered positive if the battery is discharging and negative if charging. Fig. 9 shows that the battery current resembles a scaled version of the BESS active power in Fig. 8, due to the almost constant value of the battery voltage during the simulation. The current peak is +0.3418 pu (discharging) during the +100 kW load step and –0.3023 pu (charging) during the +2 m/s wind step. The steady state current values for both steps are 0 since the system reaches the equilibrium. The battery SOC, initially set at 50%, barely changes due to the short simulation time and its relatively great capacity. The variations of the normalized battery voltage during the test are small from 1.0257 (246.17 V) to 1.0515 pu (252.36 V). These variations follow the current variations due to the internal battery resistance since SOC variations are negligible. The lowest voltage is due to the positive peak current after the +100 kW step. The highest voltage is due to negative peak current after the +2 m/s wind step. During both tests the voltage is well above the minimum permissible DC voltage for the CCI to work properly as commented in Section 4 and calculated in the Appendix.

6. Conclusions

The WDHS components modelling have been presented focusing on the BESS. Detailed schematics of CCI have been explained along with the calculations to obtain the needed battery voltage for the present application. The Ni–MH battery type has been chosen due to its high power capability, low maintenance, resistance to abuse and absence of hazardous substances. The WDHS has been tested for consumer load and wind speed steps. Comparing with the no BESS case, the BESS actuation eliminates the over/under shooting in the system frequency and IG speed, reduces the frequency peaks and voltage variations and shortens the settling time. It is possible to conclude that the BESS action under the control of the PD regulator filters the fluctuations of the wind power as well as those of the consumer loads, improving effectively the transients of the WDHS.

Appendix A. System parameters

Isolated Power System

Rated frequency, $f_{NOM} = 60$ Hz

Rated voltage (rms, phase to phase) = 480 V

Diesel Generator (DG)

DG inertia constant, $H_{DG} = 1.75$ s

Synchronous machine rated power, $P_{SM-NOM} = 300$ kVA

Wind Turbine Generator (WTG)

WTG rated power, $P_{T-NOM} = 275$ kW

WTG Inertia constant, $H_{WTG} = 2$ s

Dump Load (DL)

DL least significant bit power, $P_{STEP} = 1.4$ kW

DL rated power, $P_{D-NOM} = 357$ kW

Active Power Regulator (APR)

$f_{sampling} = 400$ Hz

Proportional gain, $K_P = 125$ kW/Hz

Derivative gain $K_D = 12.5$ kW s/Hz

Battery

Battery rated voltage = 240 V

Battery capacity = 390.625 Ah

Battery voltage model: $E = E_0 - K \frac{Q}{Q - \int idt} + A \exp(-B \int idt)$

$E_0 = 256.95$ V; $K = 3.7501$ V; $Q = 410.16$ Ah; $A = 28.80$ V;
 $B = 0.0384$ Ah⁻¹

Internal resistance = 0.0154 Ω

Filter capacity, $C = 8$ mF

Filter inductance, $L = 2.5$ μ H

Transformer

Rated power = 150 kW

Rated voltage primary/secondary-CCI side (rms, phase to phase) = 480/120 V

Transformation ratio = 4

Leakage inductance = 1.8 mH (referred to the primary side)

Three phase converter

Rated voltage $V_{L-L} = 120$ V

Rated power (BESS rated power), $P_{S-MOM} = 150$ kW

Total connection inductance = $(1.8 + 2)/4^2$ mH = 0.2375e–3 mH

Rated current = $\frac{P_n}{\sqrt{3}V_n} = 721.7$ A

Minimum V_{DC} to avoid diodes conduction = $1.10 - 1.15\sqrt{2}V_{L-L} = 187 - 195$ V

Minimum V_{DC} for rated current using SVM =

$$\sqrt{2(V_{L-L})^2 + 3(\omega Li_d)^2} = 231.74 \text{ V}$$

Minimum V_{DC} for rated current using SVM and with an overvoltage of 6% = $\sqrt{2(V_{L-L}1.05)^2 + 3(\omega Li_d)^2} = 239.29$ V

Appendix B. List of symbols

A	area swept by the Wind Turbine blades
C_p	Wind Turbine power coefficient
C_T	Wind Turbine circuit breaker
e_f	frequency error
f	system frequency
$I_{a,b,c}$	inverter phase currents
i_d	inverter direct grid current
i_q	inverter quadrature grid current
L	inverter connection coil inductance
m	inverter modulation index
N_W	Diesel Generator shaft speed measurement sensor node
N_D	Dump Load converter actuator node
N_S	Battery Energy Storage System converter actuator node
P_{D-REF}	Dump Load reference power
P_L	load power
P_{REF}	Battery Energy Storage System + Dump Load reference power
P_{S-REF}	Battery Energy Storage System reference power
P_T	Wind Turbine Generator power
P_{T-MEC}	Wind Turbine mechanical power
R	blade length
S_j	dump resistor j switch state
v	wind speed
V	inverter voltage
V_d	inverter direct grid voltage
V_q	inverter quadrature grid voltage
V_{DC}	inverter DC-link voltage
V_{L-L}	line to line RMS voltage

ω	grid pulsation
X_{D-REF}	Dump Load 8-bit binary number
ω_r	Wind Turbine shaft speed
ρ	air density

References

- [1] Wind/Diesel Systems Architecture Guidebook, American Wind Energy Association, 1991.
- [2] S. Drouilhet, High penetration AC bus wind–diesel hybrid power systems, Village Power' 98 Technical Workshop, Washington DC, Octubre 1998.
- [3] E. Muljadi, H.E. McKenna, Power quality issues in a hybrid power system, IEEE Trans. Ind. Appl. 38 (3) (2002) 803–809.
- [4] C. Carrillo, A. Feijóo, J. Cidrás, Comparative study of flywheel systems in an isolated wind plant, Renew. Energy, 2008, doi:10.1016/j.renene.2008.06.003.
- [5] R. Sebastián, R. Peña Alzola, Effective active power control of a high penetration wind diesel system with a Ni–Cd battery energy storage, Renew. Energy 35 (5) (2010) 952–965, doi:10.1016/j.renene.2009.11.029.
- [6] J.L. Rodríguez Amenedo, J.C. Burgos Díaz, S. Arnalte Gomez, Sistemas eólicos de producción de energía eléctrica, ISBN: 9788472071391, Madrid 2003.
- [7] R. Hunter, D. Infield, S. Kessler, J. de Bonte, T. Toftvaag, B. Sherwin, M. Lodge, in: Hunter, Eliot (Eds.), Designing a System. Wind–Diesel Systems: A Guide to the Technology and Its Implementations, Cambridge University Press, UK, 1994 (Chapter 4).
- [8] K.C. Divya, Jacob Østergaard, Battery energy storage technology for power systems – an overview, Electr. Power Syst. Res. 79 (4) (2009) 511–520, doi:10.1016/j.epsr.2008.09.017.
- [9] S.M. Muyeen, R. Takahashi, T. Murata, J. Tamura, H. Ali Mohd, Application of STATCOM/BESS for wind power smoothening and hydrogen generation, Electr. Power Syst. Res. 79 (2) (2009) 365–373, doi:10.1016/j.epsr.2008.07.007.
- [10] W. Lawrenz, CAN System Engineering, Springer, 1997.
- [11] The MathWorks, Inc., Simulink (built upon Matlab), Online Documentation, <http://www.mathworks.com/access/helpdesk/help/toolbox/simulink/>.
- [12] The MathWorks, Inc., “SimPowerSystems”, Simulink (built upon Matlab) Block Library Online Documentation, <http://www.mathworks.com/access/helpdesk/help/toolbox/physmod/powersys/>.
- [13] K.E. Yeager, J.R. Willis, Modelling of emergency diesel generators in an 800 Megawatt nuclear power plant, IEEE Trans. Energy Convers. 8 (September (3)) (1994) 433–441.
- [14] R. Gagnon, B. Saulnier, G. Sybille, P. Giroux, Modelling of a Generic High Penetration No-storage Wind–Diesel System Using Matlab/Power System Blockset, in: Global Windpower Conference, Paris, France, 2002, April 2002.
- [15] A.G. Tomilson, Frequency and voltage control of a high-penetration, no-storage wind–diesel system, Master Thesis, Memorial University of Newfoundland, Canada, July 1998, Available in the Internet through Library and Archives Canada/Bibliothèque et Archives Canada, http://www.nlc-bnc.ca/obj/s4/f2/dsk2/tape17/PQDD_0023/MQ36186.pdf.
- [16] P.C. Krause, O. Wasynczuk, S.D. Sudhoff, Analysis of Electric Machinery and Drive Systems, 2nd ed., Wiley-IEEE Press, 2002, February 19.
- [17] R. Sebastián, Smooth transition from wind only to wind diesel mode in an autonomous wind diesel system with a battery-based energy storage system, Renew. Energy 33 (March) (2008) 454–466 (Elsevier), doi:10.1016/j.renene.2007.03.007.
- [18] H.G. Beyer, T. Degner, H. Gabler, Operational behavior of wind–diesel systems incorporating short-term storage: an analysis via simulation calculations, Sol. Energy 54 (6) (1995) 429–439.
- [19] V. Blasko, V. Kaura, W. Niewiadowski, Sampling of discontinuous voltage and current signals in electrical drives: a system approach, IEEE Trans. Ind. Appl. 34 (September/October (5)) (1998) 1123–1130.
- [20] K. Bimal, Bose, Modern Power Electronics and AC Drives, Prentice Hall, 2002.
- [21] M. Liserre, F. Blaabjerg, A. Dell'Aquila, Step-by-step design procedure for a grid-connected three-phase PWM voltage source converter, Int. J. Electron. 91 (8) (2004) 445–460, August.
- [22] S. Drouilhet, M. Shirazi, Wales, Alaska High-Penetration Wind–Diesel Hybrid Power System. Theory of operation, NREL/TP-500-31755, May 2002.
- [23] Salvador Martinez, Alimentación de equipos informáticos y otras cargas críticas, McGraw Hill, ISBN: 84-7615-920-X, 1992.
- [24] D. Linden, T.B. Reddy (Eds.), Handbook of Batteries, 3rd ed., McGraw-Hill, ISBN: 978-0-07-135978-8, 2002.
- [25] O. Tremblay, L.-A. Dessaint, A.-I. Dekkiche, A generic battery model for the dynamic simulation of hybrid electric vehicles, in: Vehicle Power and Propulsion Conference, 2007, VPPC 2007. IEEE 9–12 September, 2007, pp. 284–289.